Chapter 4

Crystal Symmetry and Polarized Luminescence on Nonpolar ZnO

Hiroaki Matsui and Hitoshi Tabata

Additional information is available at the end of the chapter

http://dx.doi.org/10.5772/64724

Abstract

We introduce excitonic polarized photoluminescence (PL) of nonpolar ZnO layers and related quantum well (QW) structures in terms of crystal symmetries and lattice distortions. Polarized PL characters are attributed to in-plane anisotropic strains in the host, which are fully demonstrated on *A*-plane ZnO. Theoretical evaluations propose that in-plane compressive strains induced in ZnO layers play an important role in obtaining highly polarized optical properties. We experimentally achieve polarized PL responses in strain-controlled *A*-plane ZnO layers. Furthermore, we find interesting relationship between polarization degree of PL and in-plane anisotropic strains. Finally, highly polarized PL at room temperature is obtained by controlling well width in $Cd_{0.06}ZnO_{0.94}O$/ZnO QWs as a consequence of change in crystal symmetry from C_{6v} to C_{2v} at interfaces between $Cd_{0.06}Zn_{0.94}O$ well and ZnO barrier layers in the QW samples.

Keywords: ZnO, nonpolar, luminescence, anisotropy, crystal symmetry

1. Introduction

Zinc oxide (ZnO) has been one of the candidates of important materials towards the fabrications of optoelectronic platforms such as transistors, light-emitting diodes, transparent electrodes, and magnetism. ZnO has large exciton energy of 64 meV [1], which has received much attention for the possibility of utilizing excitonic-based optical applications at room temperature. In addition, MgO–ZnO and CdO–ZnO alloys are attracting great deal of interests since these alloys possess higher and lower band gaps than that of ZnO [2–6], which have been applied to $Mg_xZn_{1-x}O$/ZnO and $Cd_xZn_{1-x}O$/ZnO multiple and single quantum wells (QWs) [7–10]. These low-dimensional heterostructures can produce interesting quantum phenomena

such as an increased excitonic binding energy and two-dimensional (2D) electron transport. These physical properties have been received much attention by many researchers for science and practical applications.

ZnO has a non-centrosymmetric structure with no center of inversion. This crystal symmetry builds spontaneous and piezoelectric polarizations in the host, which provides interesting excitonic luminescence. When the growth direction is chosen along the polar [0001] axis, these polarizations result in potentially detrimental effects such as the lowering of the probability of radiative recombination of active layers in QWs due to spatial separation of electron and hole carriers because of the quantum-confinement Stark effect (QCSE) [11, 12]. To suppress the QCSE, it is needed to deposit ZnO films and quantum structures on substrates other than *Zn*-(0001) and *O*-(000-1) planes. The most promising are the nonpolar planes such as *A*-plane (11–20) and *M*-plane (10–10), which are no spontaneous polarization fields since the polar *c*-axis lies in the growth planes. Thus far, nonpolar ZnO layer growth has been performed using various oxide substrates, such as $LaAlO_3$, $LiGaO_2$, $SrTiO_3$ and (La, Sr)(Al, Ta)O_3 [13–16]. In particular, nonpolar ZnO films can be easily grown using *r*-plane sapphire substrates by pulsed laser ablation (PLD), molecular beam epitaxy (MBE), and chemical vapor deposition (CVD) [17–19]. Layer growths of nonpolar ZnO have provided some important tasks for scientific studies [20–23], which have played key factors in applying for photodetector and transistor devices [24–26]. In addition, artificial control of carrier polarity (p-type) and magnetism has also been reported [27, 28]. Accordingly, research involving ZnO has recently been focused on the growth of nonpolar axes rather than that of polar axes, which have been extended to nonpolar (*A*- and *M*-plane) $Mg_xZn_{1-x}O$/ZnO and $Cd_xZn_{1-x}O$/ZnO QWs with no internal polarization fields along the growth conditions [29, 30].

To date, some studies have reported on nonpolar ZnO-based QWs in terms of preventing the QCSE caused by *c*-polar QWs [31, 32]. The merit of nonpolar ZnO is not only the avoidance of QCSE but also the generation of polarized optical phenomena. These properties are expected to be promising for attractive optical devices such as polarized photodiodes, light-emitting diodes and solar applications [33–36]. The polarized light emissions of nonpolar ZnO are associated with the conduction (CB) and valence band (VB) levels [37]. When using nonpolar ZnO, the polarized photoluminescence (PL) of $Cd_xZn_{1-x}O$/ZnO QWs was higher than that of $Mg_xZn_{1-x}O$/ZnO QWs because the crystal symmetry in a $Cd_xZn_{1-x}O$ well layer was changed from C_{6v} to C_{2v} by introducing an anisotropic compressive strain on the growing surface [38, 39]. This lattice distortion causes a strain-induced modification of the VB, which results in polarized PL. Therefore, the polarized PL is highlighted as the consequence of anisotropic lattice distortions introduced in nonpolar ZnO layers and their related QWs.

This chapter is organized as follows. Theoretical evaluations of optical anisotropies are described in Section 2 in order to investigate polarized PL in nonpolar *A*-plane ZnO. In particular, we discuss on relationship between optical transitions at the excitonic edge and in-plane strains. In Section 3, we state film growths and polarized PL properties in nonpolar ZnO layers grown using homoepitaxial schemes. We experimentally clear correlation between polarized PL properties and in-plane strains. Furthermore, on the basis of above preliminary results, we fabricate nonpolar *A*-pane $Cd_xZn_{1-x}O$/ZnO QWs in order to show highly polarized

PL at room temperature by introducing in-plane compressive strains in the QWs, which is reported in Section 4. We report that anisotropic lattice distortions play an important role in determining the degree of polarized PL. Finally, some concluding remarks and future research directions are given in Section 5.

2. Optical polarization and electronic band structure

2.1. Electronic band calculations

Polarization control is theoretically demonstrated on the basis of excitonic selection rules at the band edge in ZnO, relating to the electronic band structures (EBSs) of the CB and VB. The transition energies of anisotropic strained *A*-plane ZnO were calculated using the $\boldsymbol{k} \cdot \boldsymbol{p}$ approximation with the 6 × 6 Bir-Pikus Hamiltonian for the VB. When treating the VBs together with the CB, we make use of the 8 × 8 Hamiltonian for the VB in combination with the 2 × 2

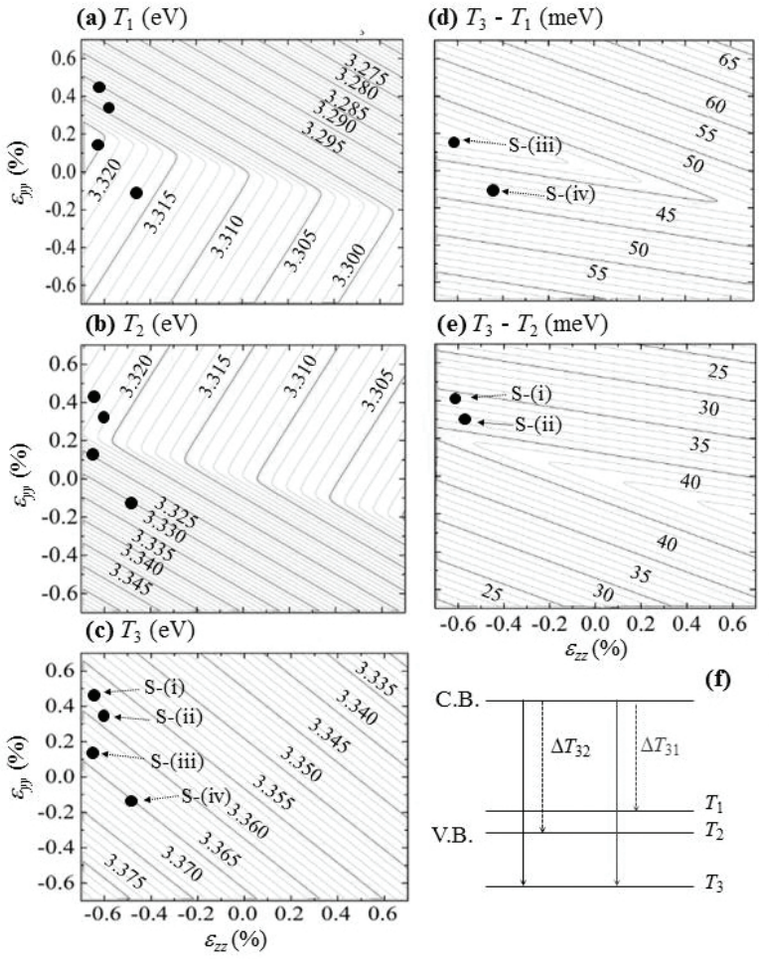

Figure 1. E_1 (a), E_2 (b), and E_3 (c) transition energies as a function of in-plane strain ε_{yy} and ε_{zz} for an *A*-plane ZnO layer at 300 K. Energy difference T_3–T_2: ΔT_{32} (d) and T_3–T_1: ΔT_{32} as a function of in-plane strain ε_{yy} and ε_{zz} (e). Schematic diagram of the transition energies of ΔT_{32} and ΔT_{31}. Black dots indicate experimental results in ZnO layers with different in-plane strains (Figure 1 of [51]). Copyright 2014 by the American Institute of Physics.

matrix for the CB. A high polarization is obtained when the energy shift (ΔE) between two inter-band transitions with $E//c$ and $E\perp c$ is large [40]. The $E//c$ and $E\perp c$ indicate electric fields parallel and perpendicular to the c-axis. We evaluated the in-plane anisotropic strains in order to obtain a large ΔE at the excitonic edge of the Γ point. For strain-free A-plane ZnO, the VBs consist of $|X \pm iY$ symmetry for the two topmost VBs (A- and B-excitons) and $|Z$ for the third VB (C-exciton). The VBs are mixed because of in-plane anisotropic strains, which provide polarized optical properties. Three transitions involving $|X$-like, $|Y$-like, and $|Z$-like VB require polarized lights along the x, y, and z directions, named T_1, T_2, and T_3 in order to increasing transition energies, respectively. The residual lattice strain $\varepsilon_{\beta\beta}$ ($\beta = x, y, z$) in the films was defined by three orthogonal directions: the x-[11-20] direction along the out-of-plane components, and the y-[1-100] direction and z-[0001] direction along the in-plane component. For calculations at 300 K, the deformation potentials D_j (j = 1–6) for the VB were given by Wrzesinski et al. [41] and Lambrecht et al. [42]. The crystal-splitting (Δ_{so}) and spin orbit splitting (Δ_{so}) were 43 and 16 meV, respectively [37]. The excitonic binding energy was taken to be 60 meV [43], and the band gap was 3.370 eV [44]. The a- and c-axis lengths were 0.3250 and 0.5204 nm, respectively [45]. The relationship between in-plane and out-of-plane strains can be expressed by the following equation [46].

$$\varepsilon_{xx} = -\frac{C_{12}}{C_{11}}\varepsilon_{yy} - \frac{C_{13}}{C_{11}}\varepsilon_{zz}. \quad (1)$$

where C_{ij} indicates the elastic stiffness constants [47]. **Figure 1a–c** shows the counter plots for variation of the transition energies T_1, T_2, and T_3 as a function of the in-plane strains. The calculations were extended to an arbitrary in-plane strain for the range $|\varepsilon_{yy}|$ and $|\varepsilon_{yy}| \leqq 0.7\%$. The energy and polarization properties of T_1, T_2, and T_3 at a zero strain are matched with those of the A-, B-, and C-excitons, respectively.

In **Figure 1**, the energy of the T_3 transition exhibits a linear correlation between ε_{yy} and ε_{zz}. In contrast, the transition energies of T_1 and T_2 showed larger energy shifts on ε_{zz} compared to ε_{yy}. The dependence of the energy shift on ε_{yy} changed in the vicinity of the boundary between tensile ($\varepsilon_{yy} > 0$) and compressive ($\varepsilon_{yy} < 0$) regions. This relation is well reflected by the oscillation strengths of T_1, T_2, and T_3 transitions (**Figure 2**). This provided a clue for an understanding of the dependence of the energy shift in each transition. However, the dependences of energy shifts of T_1, T_2, and T_3 transitions are determined by both material parameters and the relationship between ε_{xx}, ε_{yy}, and ε_{zz}. **Figure 1(d)** shows the dependence of the difference (ΔT_{31}) in transition energy $T_3 - T_1$ on the in-plane strain. An increase in ΔT_{31} was found in regions of in-plane biaxial tensile ($\varepsilon_{yy} > 0$ and $\varepsilon_{zz} > 0$) and in-plane biaxial compressive ($\varepsilon_{yy} < 0$ and $\varepsilon_{zz} < 0$) strains. On the other hand, the energy difference (ΔT_{32}) in the transition energy $T_3 - T_2$ gradually decreased in both regions of in-plane tensile and compressive strains. This result had an opposite tendency for the difference in ΔT_{31}.

The polarization anisotropy is dependent on the three polarization components of the oscillation strength for the transitions T_1, T_2, and T_3, which are obtained from momentum

http://dx.doi.org/10.5772/64724

matrix elements of the type $\varphi^c|p_l|\varphi^v$ with $l = x, y, z$ [48, 49]. The orbital part of the CB can be described as $\varphi^c| = S|$, while that of the VB can be expressed by the following equation:

$$|\varphi^v = \frac{1}{\sqrt{2}}(a_{1n} + a_{2n} + a_{5n} + a_{6n})|X + \frac{i}{\sqrt{2}}(a_{1n} + a_{2n} - a_{5n} - a_{6n})|Y + (a_{3n} + a_{4n})|Z \quad (2)$$

where the coefficients of a_{jn} (j = 1–6) were obtained from the eigenvectors of the Hamiltonian. The relative values of the oscillator strengths $S|p_x|X^2$, $S|p_{ly}|X^2$ and $S|p_z|Z^2$ are normalized to the same value [50]. The oscillator strengths for the transitions T_1, T_2, and T_3 are shown in **Figure 2**. The x polarization (out-of-plane) is not accessible with a normally incident beam when using A-plane ZnO. The oscillation strength of the T_3 transition was polarized for z polarization ($E//c$) in all strain range. However, the oscillation strengths of the T_1 and T_2 transitions changed substantially. For the in-plane biaxial compressive strains, the oscillation strength of the T_1 transition has a significant component for y polarization ($E\perp c$), providing the ΔT_{31} transition at the band edge. In contrast, the T_2 transition was polarized along the y direction for the in-plane biaxial tensile strains. Optical properties at the band edge for $E\perp c$

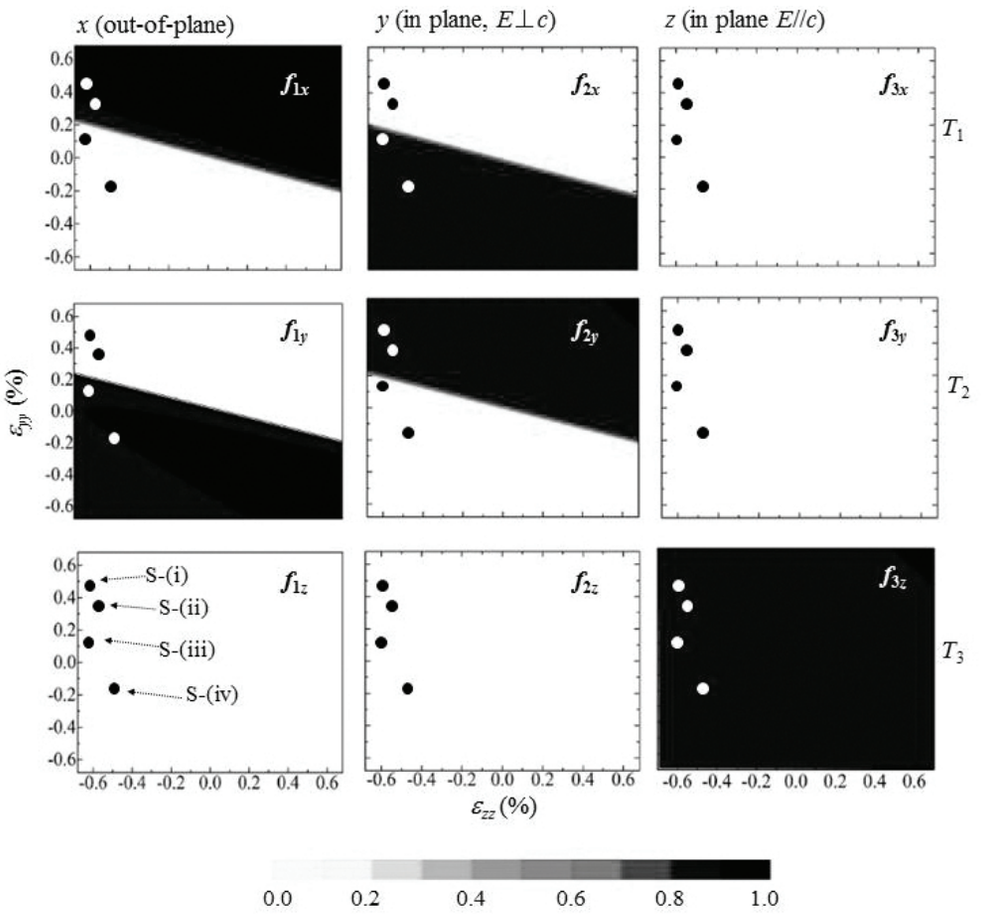

Figure 2. Relative x, y, and z components of the oscillator strength of T_1, T_2, and T_3 transitions as a function of the in-plane strain ε_{yy} and ε_{zz} of an A-plane ZnO layer. Black dots indicate experimental results in ZnO layers with different in-plane strains (Figure 2 of [51]). Copyright 2014 by the American Institute of Physics.

and $E//c$ consisted of a single inter-band transition. A large ΔE was observed within regions of in-plane biaxial compressive strains in *A*-plane ZnO.

2.2. In-plane strains and crystal symmetries

A-plane ZnO layers were deposited on sapphire (10-12) substrates using PLD. ArF excimer laser pulses (193 nm, 1 J/cm^2 and 3 Hz) were focused on ZnO targets (99.999%: 5 N) located 4 cm from the substrates in an oxygen flow of 1.8×10^{-2} Pa. The substrate temperatures were changed within the range of 450–730°C. ZnO layers grown at 450, 550, 650, and 730°C were named to S-(i), S-(ii), S-(iii), and S-(iv), respectively [51].

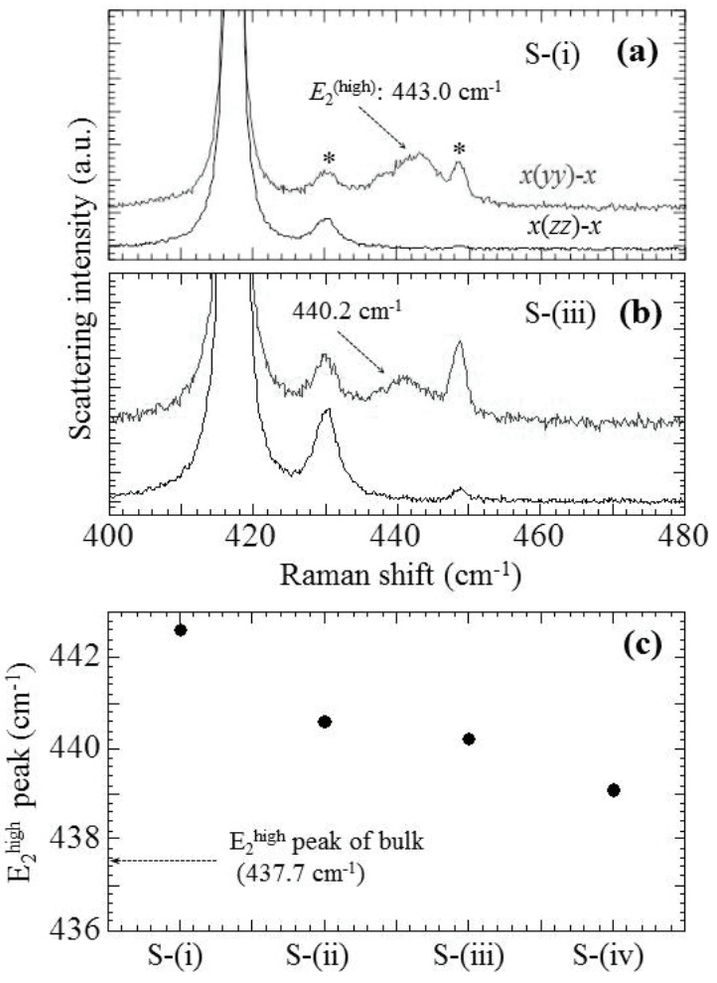

Figure 3. Polarized Raman spectra for ZnO layers at T_g = 450 (a) and 650°C (b) measured in two distinct backscattering geometries. Raman peaks of the sapphire substrate are indicated by*. (c) Peak frequency of E_2^{high} mode in ZnO layers at different in-plane strains (Figure 3 of [51]). Copyright 2014 by the American Institute of Physics.

We investigated crystallographic polarizations of the layers using micro-Raman scattering. The polarized Raman scattering was measured in two distinct backscattering geometries under a 514.5 nm laser at 300 K. We select the E_2^{high} peak based on the A_{1g} mode located at around 442

cm^{-1}. The E_2^{high} peak was found in the $x(yy)$-x geometry (**Figure 3a** and **b**). In contrast, we could not confirm the E_2^{high} peak in the $x(zz)$-x geometry due to crystal symmetry of nonpolar ZnO. In addition, the E_2^{high} peak is very sensitive to the in-plane strains, and their positions of all layers shifted to high-frequency region as compared to that of strain-free *A*-plane ZnO (**Figure 3c**). The frequency shift ($\Delta\omega$) of the E_2^{high} peak can be described as follows [52].

$$\Delta\omega = a(\varepsilon_{xx} + \varepsilon_{yy}) + b\varepsilon_{zz} \pm c(\varepsilon_{xx} + \varepsilon_{yy}) \tag{3}$$

where the coefficients of *a*, *b*, and *c* represent the corresponding deformation potentials per unit strain. In Eq. (3), the red-shifted E_2^{high} peak cleared presence of a compressive strain in the layer.

The lattice parameters of the layers were determined by high-resolution x-ray diffraction (HR-XRD). ZnO layers deposited at different T_g produced various in-plane strains. Large compressive strains along the *c*-axis direction were observed in all layers, which were also supported from the Raman data. All layers had orthorhombic distortion of C_{2v} symmetry. The relationship between the in-plane and out-of-plane strains was satisfied with Eq. (1) in all layers, which makes it possible to compare theoretical and experimental results. The layers grown at below T_g = 650°C showed compressive and tensile strains along the *z*- and *y*-directions. The values of (ε_{yy} and ε_{zz}) of the layers at T_g = 450, 550, and 650°C were (+0.42% and −0.61%), (+0.27% and −0.56%), and (+0.15% and −0.65%), respectively. On the other hand, the layer at T_g = 730°C realized in-plane biaxial compressive strains (ε_{yy} = −0.11% and ε_{zz} = −0.46%). Details were reported to Ref. [32].

2.3. In-plane strains and optical absorptions

Polarized absorption spectra were measured for the $E\perp c$ ($\alpha_\perp$) and $E//c$ ($\alpha_{//}$) geometries. **Figure 3** shows significant polarization anisotropy at the band edge. A plot of α^2 as a function of energy *E* for the ZnO layers at T_g = 450°C [S-(i)] showed that the absorption edge shifted to higher energy for $E//c$ relative to $E\perp c$ by 18 meV. The lines can be fitted by the following equation for direct interband transition:

$$\alpha^2(E) = \beta^2[E - E_{exp}] \tag{4}$$

where the values of β for both polarizations are related to oscillation strengths. We obtained the extrapolated absorption edge (E_{exp}) of 3.320 and 3.3378 eV for $E\perp c$ and $E//c$, respectively (**Figure 4a**). The energy separation (ΔE) at the absorption edge for $E\perp c$ and $E//c$ indicates the difference in the band gap. Values of E_{exp} for a layer at T_g = 650°C [S-(iii)] were 3.321 and 3.353 eV for $E\perp c$ and $E//c$, respectively (**Figure 4b**), resulting in an increased ΔE of 32 meV. The highest ΔE of 42 meV was obtained in the layer at T_g = 730°C [S-(iv), **Figure 4c**]. Herein, the transition energies in layers at T_g = 450°C [S-(i)] and 550°C [S-(ii)] were defined by T_2 and T_3 transitions, which dominated the optical transitions for $E\perp c$ and $E//c$, respectively. In contrast,

E_{exp} values for $E \perp c$ and $E//c$ in layers at T_g = 650°C [S-(iii)] and 730°C [S-(iv)] were equivalent to the T_1 and T_3 transitions, respectively. Therefore, a decrease in ε_{yy} resulted in the change of the inter-band transitions from ΔT_{32} to ΔT_{31}. The large ΔE at the band edge was caused by the energy difference between T_1 and T_3 transitions (**Figure 4c**).

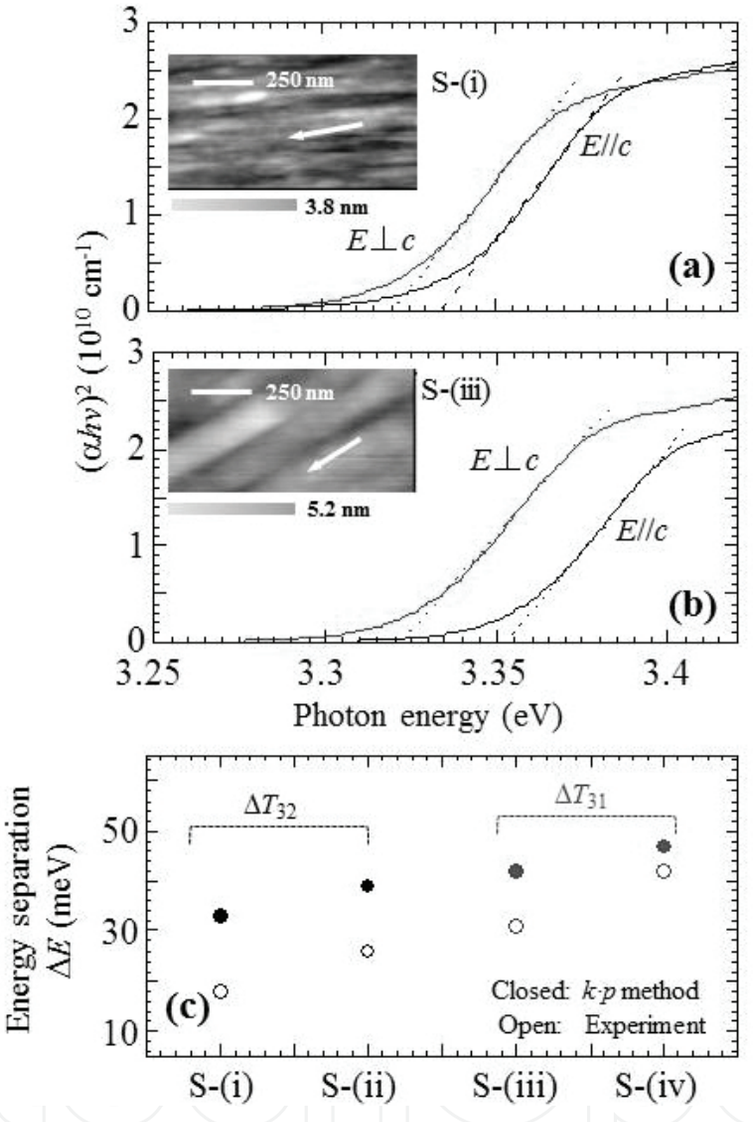

Figure 4. α^2E^2 as a function of photon energy E and AFM image (inset) in a ZnO layer at T_g = 450°C (a) and T_g = 650°C (b). (c) Correlation between experimental ΔE and theoretical ΔT between the two polarization directions for ZnO layers at different in-plane strains (Figure 4 of [51]). Copyright 2014 by the American Institute of Physics.

In this section, we theoretically investigated relationship between energy separations and in-plane anisotropic strains on *A*-plane ZnO, which were sufficiently verified from the experimental results. The large ΔE at the band edge was obtained by introducing the in-plane compressive strains in the layers, providing the large difference in absorption measured in the $E//c$ and $E \perp c$ geometries. It is expected that the introduction of in-plane compressive strains into *A*-plane ZnO can produce highly polarized PL.

3. In-plane lattice strains and polarized luminescence

3.1. *A*-plane ZnO homoepitaxial layer growth

We report homoepitaxial growth for strain-free and strained *A*-plane ZnO layers from viewpoints of morphologies, structural and optical properties. In particular, we present relationship between polarized PL and in-plane lattice strains because any in-plane anisotropic strain changes the crystal symmetry in the layers in terms of significant modifications of the EBS of ZnO.

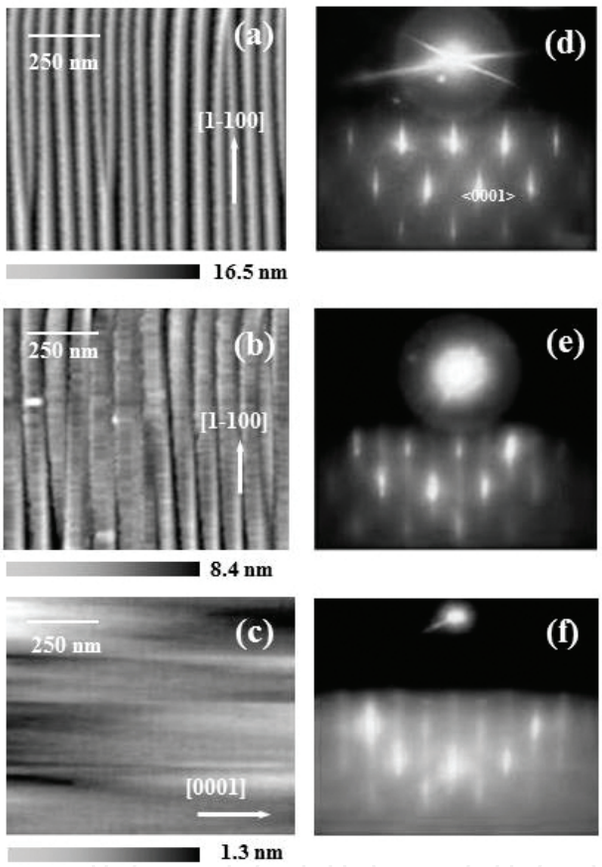

Figure 5. AFM images of strain-free ZnO layers with thicknesses of (a) 10 nm, (b) 28 nm, and (c) 140 nm. RHEED patterns with the [0001] azimuth of strain-free ZnO layers with thicknesses of (d) 10 nm, (e) 28 nm, (f) 140 nm (Figure 1 of [53]). Copyright 2012 by the American Institute of Physics.

The hydrothermally synthesized substrates were supplied by Crystec GmbH (Germany) and Goodwill (Russia). Both substrates were annealed at 1100°C for 1 h prior to PLD growth. *A*-plane ZnO layers were homoepitaxially grown on both substrates at 550°C in an oxygen flow of 10^{-4} mbar. ArF excimer laser pulses were focused on a ZnO target (5 N) 4.0 cm from the substrate [53].

Growth processes of the homoepitaxial layers on Crystec ZnO substrates were monitored using reflection high electron energy diffraction (RHEED) with the [0001] azimuth. Atomic force

microscopy (AFM) was used to observe surface morphologies. At the beginning of layer growth, up to 10 nm in thickness, the V-groove was seen with a RHEED pattern of three-dimensional (3D) spot (**Figure 5a** and **d**). However, continued layer growth of ZnO up to 28 nm, changed to a slightly smooth surface by the filling of the V-groove structure (**Figure 5b**). As a consequence, the 3D spot of the RHEED pattern were weakened (**Figure 5c**). Finally, the layer morphology at a thickness of 140 nm showed a very flat surface. The RHEED pattern showed a sharp blight stripe with a high contrast to the background, which resulted from a clean and smooth surface (**Figure 5c** and **f**).

A cross-sectional transmittance electron microscopy (X-TEM) image with the [0001] zone axis showed that layer surface had nano-facet structures (**Figure 6a** and **b**). The nano-facets were consisted of the *M*-plane from the angle between the nano-facets and (11-20) plane due to higher surface energy of *A*-plane ZnO than *M*-plane ZnO (**Figure 6d**) [54]. The XRD showed that the 2θ pattern of the (11-20) plane was accompanied by Pendellosung fringes, which is related to interference between the layer surface and the layer/substrate interface. The XRD profile cleared coherent growth of *A*-plane ZnO.

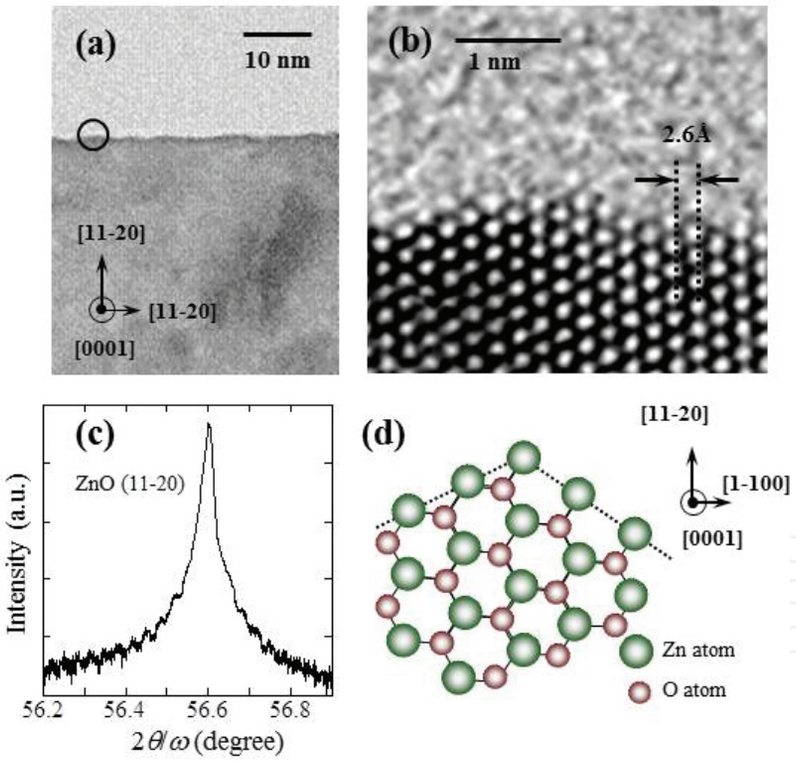

Figure 6. (a) Low-magnification and (b) high-magnification X-TEM images of a strain-free ZnO layer with a thickness of 140 nm. (c) Schematic cross-section of the atomic lattice of ZnO viewed along the [0001] direction (Figure 2 of [53]). Copyright 2012 by the American Institute of Physics.

Strained *A*-plane ZnO layers could be obtained using the goodwill ZnO substrates. The 2θ pattern of the (11-20) plane was separated from that of the ZnO substrate. The out-of-plane strain (ε_{xx}) expanded 0.47% with x being parallel to the [11-20] direction (**Figure 7a**). In addition,

the layer showed a broad ω-rocking curve with a line-width of 0.14° because of a lattice relaxation at the heterointerface (**Figure 7b**). As a result, the in-plane lattice strain (ε_{yy} and ε_{zz}) showed anisotropic compressions of 0.04 and 0.78%, with *y* and z, respectively, being parallel to the [10-10] and [0001] direction. These values were determined from reciprocal space mapping of the (0002) and (10-10) planes (**Figure 7c** and **d**). For the local strain in *A*-plane wurtzite, ε_{xx} can be expressed using Eq. (1). The calculated ε_{xx} was estimated as +0.42%, which was close to the experimental ε_{xx}. The lattice expansion along the [11-20] direction resulted from the anisotropic compressive strains along the in-plane directions.

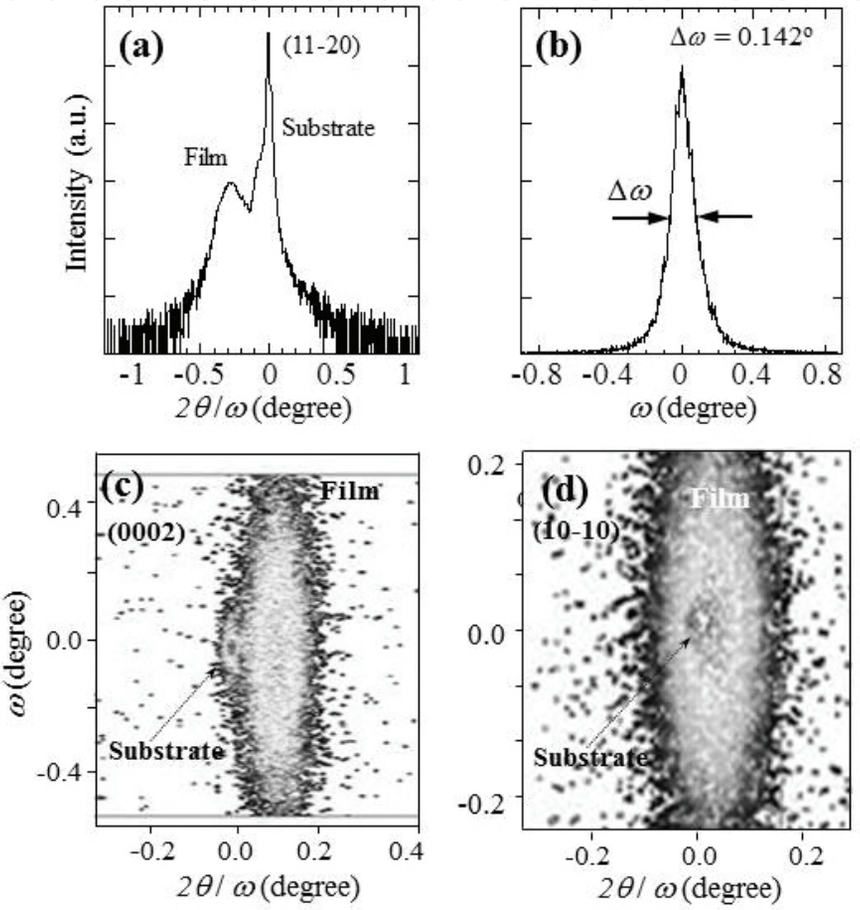

Figure 7. (a) $2\theta/\omega$ and (b) ω-rocking profiles of the (11–20) plane for strained ZnO layers. Reciprocal space mapping of (c) (0002) and (d) (10–10) for the strained ZnO layer (Figure 3 of [53]). Copyright 2012 by the American Institute of Physics.

3.2. Polarized PL from anisotropic strained ZnO layers

The in-plane lattice strains were highlighted to polarized PL. An oxygen pressure [$p(O_2)$] during the PLD growth could successfully produce the different lattice strains. The value of ε_{xx} gradually increased with increasing $p(O_2)$. In contrast, the values of ε_{yy} and ε_{zz} decreased. The relationship between ε_{xx}, ε_{yy}, and ε_{zz} was consistent with the theoretical calculation [Eq. (1)]. The increased ε_{xx} along the *x* direction was attributed to the anisotropic compressive strains

along the in-plane (y – z) directions. The VBs of ZnO consist of p-like orbitals with wave functions of $|X \pm iY\rangle$ states for Γ_9 and $\Gamma_{7\text{upper}}$ bands and a $|Z\rangle$ state for the $\Gamma_{7\text{low}}$ band. The lowest A-exciton (Γ_9) occurs because of $E \perp c$, while the C-exciton ($\Gamma_{7\text{low}}$) occurs at the higher energy under $E//c$ [37].

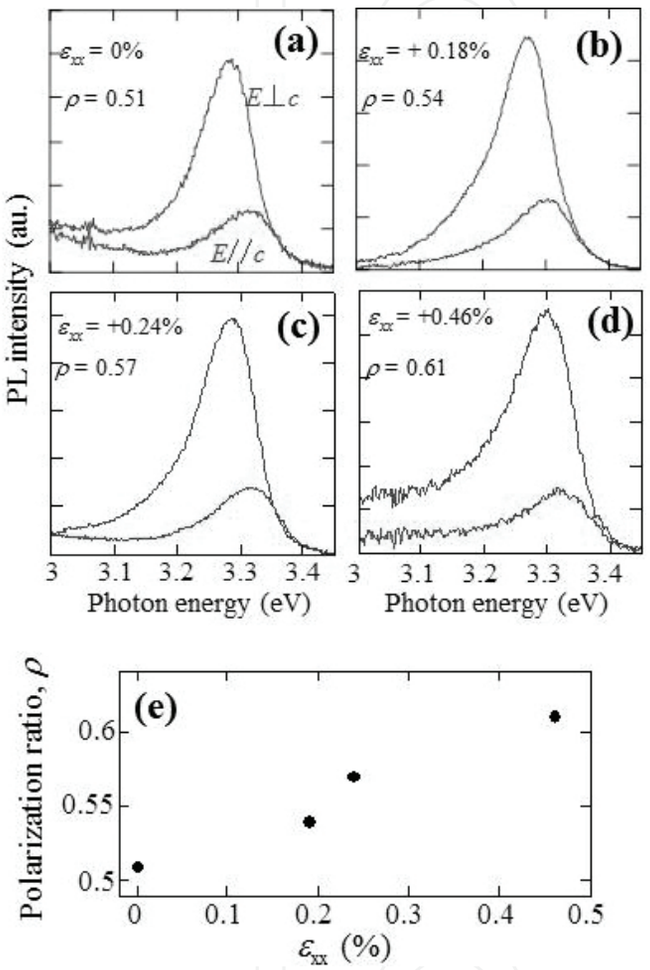

Figure 8. (a) Polarized PL spectra of a strain-free ZnO layers. Polarized PL spectra of strained layers with ε_{xx} = +0.19% (b), +0.24% (c), and +0.46% (d). (e) Polarized ratio (ρ) as a function of lattice strain (ε_{xx}) (Figure 5 of [53]). Copyright 2012 by the American Institute of Physics.

The strain-free ZnO layer showed polarization to $E \perp c$ with a polarization ratio (ρ) of 0.51 (**Figure 8a**). A value of ρ can be expressed by the following relation:

$$\rho = \frac{I_{\perp} - I_{//}}{I_{\perp} - I_{//}} \tag{5}$$

where $I_{\perp}$ and $I_{//}$ indicate the peak intensities for $E \perp c$ and $E//c$, respectively. Peak energies of PL were determined as 3.286 and 3.327 eV at 300 K for $E \perp c$ and $E//c$, respectively, which resulted

in an energy separation (ΔE) of 41 meV. This value was close to the theoretical value between *A*- and *C*-excitonic transitions. The PL intensities of all strained ZnO layers were polarized to $E \perp c$ (**Figure 8b–d**). In-plane anisotropic strains change the EBS of ZnO. The original $|X \pm iY$ states are separated into $|X$-like and $|Y$-like states. The $|Y$-like state is raised, while that of the $|X$-like state is lowered. Therefore, a large polarization ratio of PL would be measured by the large energy separation between $|Y$-like state and $|Z$-like states for $E \perp c$ and $E//c$, respectively. The strained *A*-plane ZnO layers showed the blueshift of the PL peak energy when changing from $E \perp c$ to $E//c$. ρ gradually increased by up to 0.62 with increasing out-of-plane strain (ε_{xx}) (**Figure 8e**) because photo-excited holes occupy $|Y$-like and $|Z$-like states of the VBs by the Boltzmann-like distribution. The increase in ρ reflects a large difference in transition energies for $E \perp c$ to $E//c$, which originated from a lift of the degeneracy of VB with the anisotropic compressive strains. The degree of PL polarization was well correlated with the in-plane anisotropic strains.

In this section, the in-plane anisotropic strains were introduced in *A*-plane ZnO layers by changing substrate-type and growth condition. Strain-free layers were obtained when using Crystec ZnO substrates, while the use of Goodwill ZnO substrates provided strained ZnO layers. The magnitude of lattice strain was systematically changed by controlling the oxygen pressure during the PLD growth. The correlation between PL polarization and in-plane anisotropic strain was evidenced experimentally.

4. Control of polarized luminescence by quantum well geometries

4.1. $Cd_xZn_{1-x}O$/ZnO quantum wells

The anisotropic lattice distortion causes strain-induced modification of the EBS in ZnO, leading to polarization modulation of PL. That is, polarization ratio of PL is strongly highlighted by the anisotropic lattice distortion introduced in nonpolar ZnO. In this section, we report on quantum size effects of polarized PL on *A*-plane $Cd_xZn_{1-x}O$/ZnO QWs. A change in a quantum well width of a QW has a remarkable influence on a quantum size effect. There is a strong quantum confinement following a narrowing of well width (L_W). In our work, we observe highly polarized PL from *A*-plane $Cd_{0.06}Zn_{0.94}O$/ZnO QWs when using a narrow well width [30]. This finding suggests that a valence sub-band and a corresponding thermal carrier distribution are dependent on well width. The $Cd_{0.06}Zn_{0.94}O$ well layer is very sensitive to an epitaxial lattice strain owing to lattice mismatch between $Cd_{0.06}Zn_{0.94}O$ well and ZnO layers. The contribution of well width to the optical properties on *A*-plane $Cd_{0.06}Zn_{0.94}O$/ZnO QWs becomes very important to achieve highly polarized PL at room temperature.

$Cd_{0.06}Zn_{0.94}O$/ZnO QWs with different L_W were grown on *A*-face ZnO substrates by PLD. A $Cd_{0.06}Zn_{0.94}O$ well layer was embedded between a 150 nm-thick ZnO buffer and 5 nm-thick ZnO capping layers. The ZnO buffer was deposited at T_g = 650°C, while the well and capping layers were both grown at T_g = 260°C. An AFM image of an *A*-plane QW with L_W = 4.8 nm showed that the morphology of ZnO capping of the QW showed a small surface undulation elongated along the [0001] direction due to the anisotropic migrations of adatoms on the

growing surface (**Figure 9a**) [55–57]. The height scale in the image was 1.4 nm with a roughness of a few angstroms, which was also confirmed using RHEED with a streaky pattern (**Figure 9b**). The whole specimens gave the same surface states, being independent of well width. The scanning electron microscopy (STEM) image with the [0001] zone axis revealed that an interface between the well and barrier layers was very smooth (**Figure 9c**). Therefore, we could keep the structural disorder of the interface between the barrier and the well layers to a minimum, which can reduce a partial loss of polarization deriving from the breaking of the selection rule owing to the structural disorder at the interface.

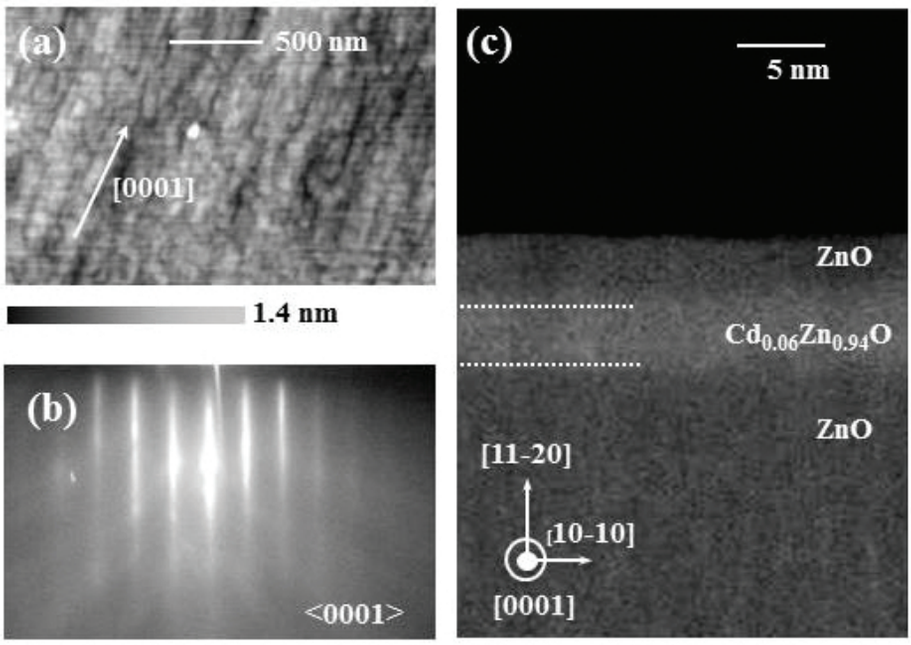

Figure 9. (a) AFM image and (b) RHEED pattern of a QW with L_W = 4.8 nm. (c) Cross-sectional STEM image taken along the [0001] zone axis of a QW with L_W = 4.8 nm (Figure 1 of [30]). Copyright 2012 by the American Institute of Physics.

4.2. Polarized PL properties in *A*-plane $Cd_{0.06}Zn_{0.94}O$/ZnO QWs

Figure 10a and **b** shows polarized PL spectra of a QW with L_W = 4.8 and 2.0 nm. The PL intensity for $E \perp c$ was higher than that for $E//c$. Energy separations (ΔE) between PL peak energies of $E \perp c$ and $E//c$ were 41 and 47 meV for QWs with L_W = 4.8 and 2.0 nm, respectively. These values were larger than that for the strain-free ZnO layer (ΔE: 35 meV). The large ΔE values are attributed to the strain-induced modification of the EBS in ZnO. In particular, the VB band is separated to three levels: $|Y$-like, $|Z$-like, and $|X$-like states in order to decrease energy by introducing anisotropic compressive strains on the growing surfaces of well layers. The y-($E \perp c$) and z-polarized ($E//c$) light components are dominated by the $|Y$-like and $|Z$-like states, respectively.

The polarization ratio (ρ) of the PL intensity for $E \perp c$ and $E//c$ was dependent on temperature (T) (**Figure 10c** and **d**). Excited carriers (electrons and holes) at 300 K fully distributed

http://dx.doi.org/10.5772/64724

in the $|Z$-like state, providing ρvalues of 0.63 and 0.71 for QWs with an L_W of 4.8 and 2.0 nm, respectively. The values of ρ gradually increased with decreasing T because the distributions of holes in the $|Y$-like state was higher than that in the $|Z$-like state. The high ρ of 0.82 and 0.88 was observed at 200 K by a negligible carrier distribution in the $|Z$-like state. The driving force to elevate carriers up to the $|Z$-like state is related to k_BT. When two different VB bands with the same effective mass are separated by ΔE, and carriers obey a Boltzmann-like distribution. ρ is described by the following expression [58]:

$$\rho = \frac{1-\exp(-\frac{\Delta E}{k_B T})}{1-\exp(-\frac{\Delta E}{k_B T})} \tag{6}$$

The calculated ΔE was 41 and 45 meV for QWs with L_W = 4.8 and 2.0 nm, respectively. These values were close to the experimental ΔE obtained from polarized PL spectra at 300 K (**Figure 10c** and **d**). Optical anisotropy for a temperature in the range 200–300 K obeys the

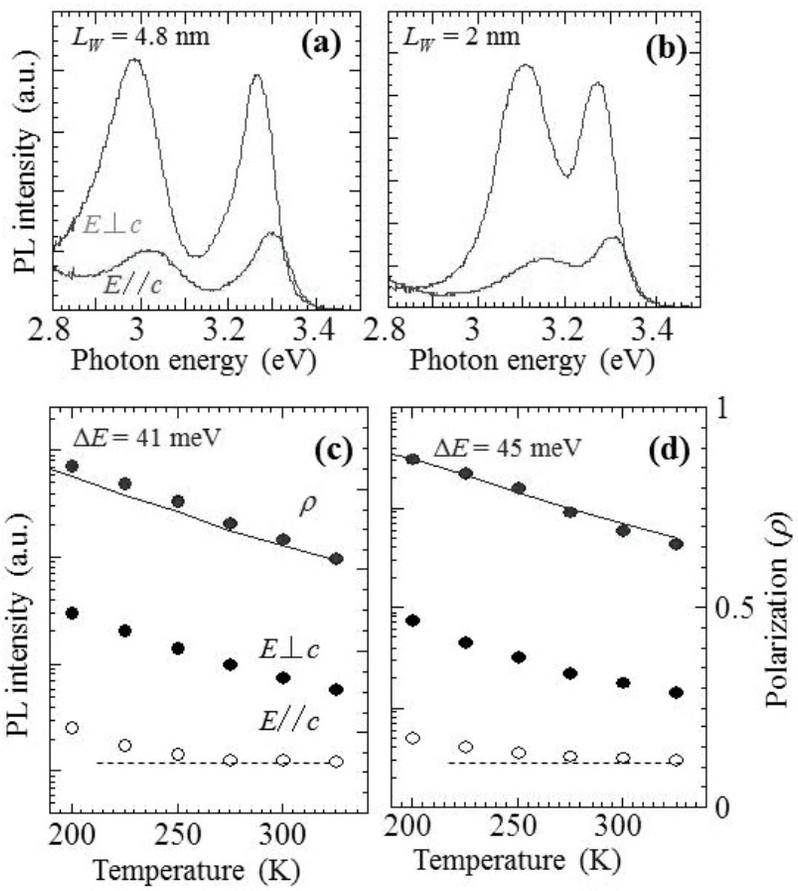

Figure 10. Polarized PL spectra at 300 K of a QW with LW = 4.8 nm (a) and 2.0 nm (b) for $E\perp c$ and $E//c$. Temperature dependence of PL peak energy for $E\perp c$ and $E//c$ and polarization (ρ) on QWs with L_W = 4.8 nm (c) and 2.0 nm (d) (Figure 2 of [30]). Copyright 2012 by the American Institute of Physics.

polarization selection rule based on a Boltzmann-like distribution. On the other hand, this selection rule breaks at low temperatures below 200 K because of the weak mixing between the different VB states, which is related to excitonic localization in the well layers [59].

4.3. Control of polarized PL in the QWs

Figure 11a shows the PL peak energies of QWs at 300 K as a function of well width. The PL peak energies systematically shifted to the higher energy with decreasing L_W because of quantum confinement. In our QW samples, no shift was observed when varying the excitation power from 0.1 to 10 W/cm^2, indicating no carrier screening effect owing to the absence of QCSE along the nonpolar growing direction. These trends were similar to those reported earlier for homoepitaxial ZnO/$Mg_xZn_{1-x}O$ QWs on nonpolar ZnO substrates. Moreover, PL peak energies at 300 K for QWs with L_W = 2.8 and 6 nm are also applicable to Eq. (6) because

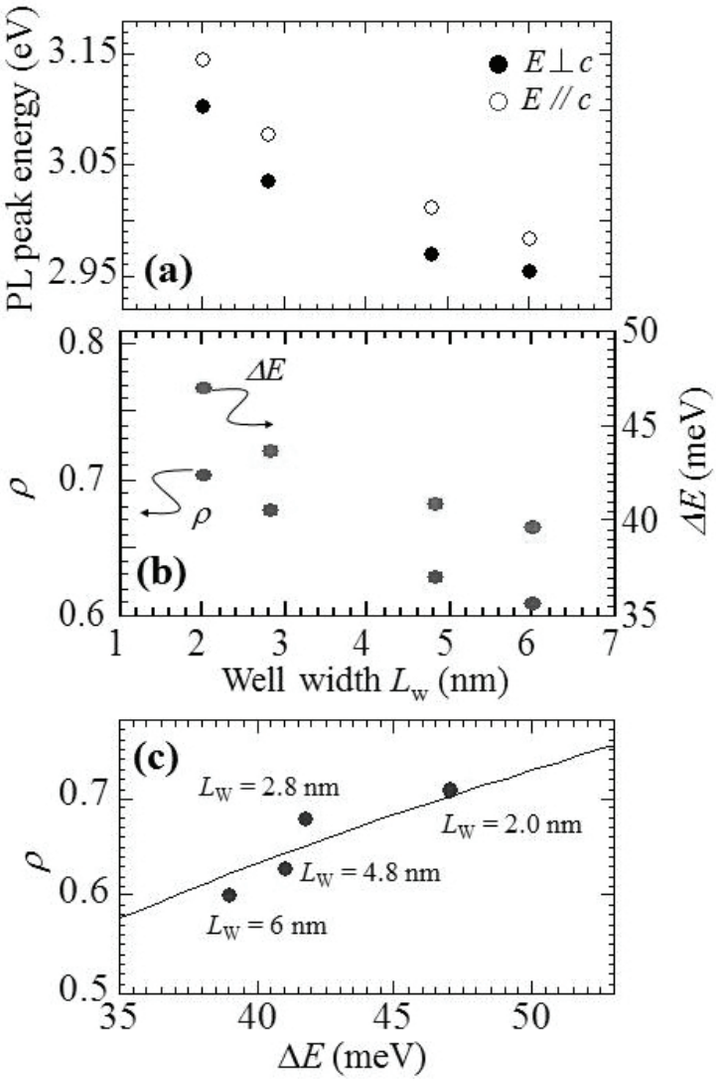

Figure 11. (a) Dependence of PL peak energy at 300 K for $E \perp cs$ and $E//c$ on L_W. (b) Dependence of ΔE and ρ on L_W at 300 K. (c) Correlation between ΔE and ρ in A-plane $C_{d0.06}Zn_{0.94}O$/ZnO QWs with different L_W. The solid line is described using Eq. (6) (Figure 3 of [30]). Copyright 2012 by the American Institute of Physics.

localization of excitons was 10.2 and 9.8 meV in QWs with L_W = 2.8 and 6.0 nm, respectively. Tuning of L_W in a QW influenced ΔE and ρ of the polarized PL at 300 K. **Figure 11b** shows the values of ρ and ΔE between the topmost VB levels as a function of L_w. At 300 K, ρ and ΔE gradually decreased with a widening of L_W and acquired values as low as 0.61 and 39 meV, respectively, when L_w was set to 6.0 nm. The values of ρ and ΔE were strongly dependent on a L_W. In order to investigate the cause of this dependence, we plotted the correlation between ρ and ΔE using Eq. (6). The calculated fit the experimental data quite well (**Figure 11c**). This indicated that the PL anisotropy of all QWs was derived from the selection rule based on a Boltzmann-like distribution. The energy separation of the topmost VB levels determined the polarization ratio of QWs.

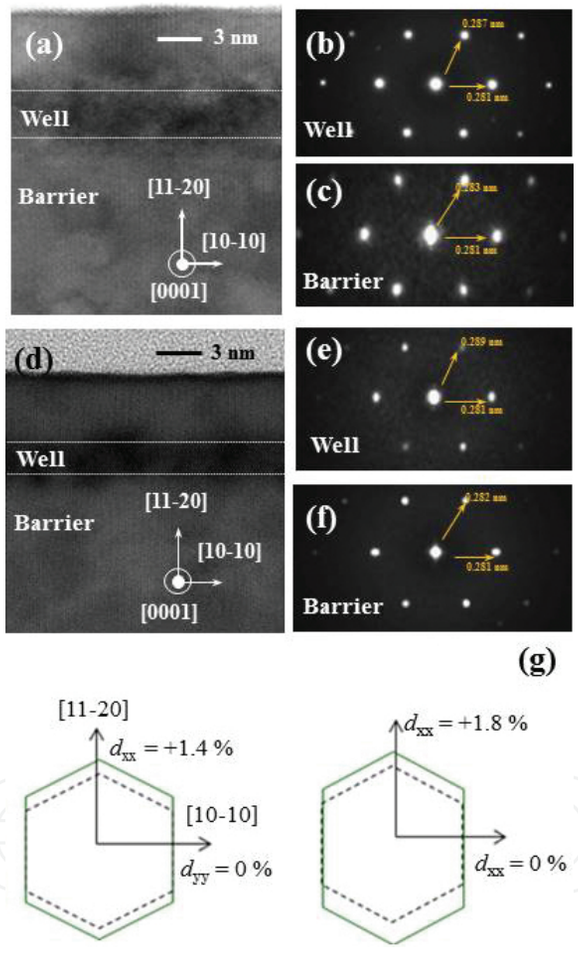

Figure 12. (a) Cross-sectional TEM image of a QW with L_W = 4.8 nm, and RSD patterns taken in the well (b) and barrier layer (c) regions. (d) Cross-sectional TEM image of a QW with L_W = 2.0 nm and RSD patterns taken in the well and barrier layers. (g) Schematic cross-section of a ZnO host viewed along the [0001] direction. The black dot and green solid lines represent ZnO layers and lattice disordered $Cd_{0.06}Zn_{0.94}O$ layers in QWs with L_W = 4.8 and 2.0 nm, respectively (Figure 4 of [30]). Copyright 2012 by the American Institute of Physics.

TEM images of QWs with L_W = 4.8 and 2.0 nm are shown in **Figure 12a** and **d**, respectively. The location of well layers in the QWs was identified by *z*-contrast STEM images. A fast Fourier transform (FFT) analysis was performed to examine a plane interval on the basis of a reciprocal

space diffractogram (RSD) pattern. The plane intervals (d_{xx}) along the *x*-axis in the well layers were 1.65 and 1.66 Å for QWs with L_W = 4.8 and 2.0 nm, respectively. For a QW with L_W = 4.8 nm, the value of d_{xx} in the well layer expanded by 1.4% compared with that in the barrier layer (**Figure 12b** and **c**). Expansion of d_{xx} to the order of 1.8% was obtained for a QW with L_W = 2.0 nm (**Figure 12e** and **f**). In contrast, the in-plane intervals (d_{yy}) of the well layer were consistent with those of barrier layers for both QWs. As a consequence, the plane intervals along the *x*-axis only increased with a narrowing of L_W, which resulted in anisotropic lattice distortions of the basal hexagon of the $Cd_{0.06}Zn_{0.94}O$ unit cell in the well layers as shown schematically in **Figure 12g**.

Makino et al. reported lattice parameters of relaxed $Cd_xZn_{1-x}O$ (up to x = 0.073) epitaxial layers on $ScMgAlO_4$ substrates [60]. From their estimations, lattice parameters of *a*- and *c*-axis lengths at x = 0.06 are calculated as 3.260 and 5.241 Å, respectively, which indicates the *a*-axis length of $Cd_{0.06}Zn_{0.94}O$ slightly expanded by 0.3% compared to that of ZnO. Thus, the lattice distortions of well layers are larger than those of relaxed $Cd_xZn_{1-x}O$ layers, which lead to a change of structural symmetry from C_{6v} to C_{2v}. It is thought that the anisotropic lattice distortions along the growing direction are related to anisotropic compressive strains on the in-plane growing surfaces. Mata et al. reported that the highly polarized PL of *a*-plane GaN/AlN QWs exhibited a narrowing of L_W because of the increased anisotropic lattice distortions in the GaN well layers [61]. Moreover, the in-plane optical anisotropy was found even in (001) zinc-blende GaAs/AlGaAs QWs when its D_{2d} symmetry is reduced to C_{2v} in the GaAs well layers [62]. Accordingly, the highly polarized PL resulting from quantum confinement in *a*-plane $Cd_{0.06}Zn_{0.94}O$/ZnO QWs is associated with the anisotropic lattice distortions of well layers giving the change of crystal symmetry. This phenomenon is derived from an increase in the energy separation between the two topmost VB levels in the well layers of the QWs.

In this section, the dependence of polarized PL on well width was studied in *A*-plane $Cd_{0.06}Zn_{0.94}O$/ZnO QWs. The polarization ratio of PL gradually enhanced with a narrowing of L_W, resulting from the energy separation between the two topmost VB states. These effects were a result of the anisotropic compressive distortions in the well layers. The lattice distortions in the well layers played an important role in determining the degree of polarized PL, which could be controlled by well width.

5. Conclusion remarks

This chapter was reported polarized PL of nonpolar ZnO layers and their QW structures in terms to the crystal symmetry and the in-plane lattice strain during PLD growth. Anisotropic optical properties were closely related to in-plane anisotropic strains introduced into the layers, which were demonstrated on *A*-plane ZnO. Overall, the in-plane compressive strains could obtain highly anisotropic optical properties from consistency between experimental and theoretical viewpoints. We actually observed the polarized PL spectra at 300 K in the strain-controlled *A*-plane ZnO homoepitaxial layers. Furthermore, we showed systematic correlation

between the polarization degree of PL and the in-plane lattice strain. Finally, we achieved highly polarized PL at room temperature by controlling a well width in the QW structures as a consequence of change in crystal symmetry from C_{6c} to C_{2v} at a hetero interface between the well and barrier layers.

Acknowledgements

This work was supported in part by a grant-in-aid from the JSPS Core-to-Core Program, A. Advanced Research Network, a grand from the Japan Science and Technology Agency (JST: A-Step) and a grant-in-aid from Exploratory Research and Scientific Research (B).

Author details

Hiroaki Matsui[1*] and Hitoshi Tabata[2]

*Address all correspondence to: hiroaki@ee.t.u-tokyo.ac.jp

1 Department of Bioengineering, The University of Tokyo, Bunkyō, Japan

2 Department of Electric Engineering and Information Systems, The University of Tokyo, Bunkyō, Japan

References

[1] D. G. Thomas. The exciton spectrum of zinc oxide. Journal of Physical and Chemical Solids. 1960;15:86–89. doi:10.1016/0022-3697(60)90104–9

[2] A. Ohtomo, M. Kawasaki, T. Koida, K. Masubuchi, H. Koinuma, Y. Sakurai, Y. Yoshida, T. Yasuda and Y. Segawa. $Mg_xZn_{1-x}O$ as a II–VI widegap semiconductor alloy. Applied Physics Letters. 1998;72:2466–2468. doi:10.1063/1.121384

[3] T. Gruber, C. Kircher, R. Kling, F. Reuss, A. Waag, F. Bertram, D. Forster, J. Christen and M. Schreck. Optical and structural analysis of ZnCdO layers grown by metalorganic vapor-phase epitaxy. Applied Physics Letters. 2003;83:3290–3292. doi: 10.1063/1/1620674

[4] S. Sadofev, P. Schäfer, Y. H. Fan, S. Blumstengel, F. Henneberger, D. Schulz and D. Klimm. Radical-source molecular beam epitaxy of ZnMgO and ZnCdO alloys on ZnO substrates. Applied Physics Letters. 2007;91:201923(1)–(3). doi:10.1063/1.2815662

[5] F. Bertram, S. Giemsch, D. Forster, J. Christen, R. Kling, C. Kirchner and A. Waag. Direct imaging of phase separation in ZnCdO layers. Applied Physics Letters. 2006;88:061915(1)–(3). doi:10.1063/1.2172146

[6] M. D. Neumann, C. Cobet, N. Esser, B. Laumer, T. A. Wassner, M. Eickhoff, M. Feneberg and R. Goldhan. Optical properties of MgZnO alloys: Excitons and exciton-phonon complexes. Journal of Applied Physics. 2011;110:013520(1)–(8). doi:10.1063/1.3606414

[7] T. Makino, C. H. Chia, N. T. Tuan, H. D. Sun, Y. Segawa, M. Kawasaki, A. Ohtomo, K. Tamura and H. Koinuma. Room-temperature luminescence of excitons in ZnO/(Mg, Zn)O multiple quantum wells on lattice-matched substrates. Applied Physics Letters. 2000;77:975–977. doi:10.1063/1.1289066

[8] A. Y. Azariv, T. C. Zhang, B. G. Svensson and A. Y. Kuznetsov. Cd diffusion and thermal stability of CdZnO/ZnO heterointerfaces. Applied Physics Letters. 2011;99:11903(1)–(3). doi:10.1063/1.3639129

[9] T. Makino, A. Ohtomo, C. H. Chia, Y. Segawa, H. Koinuma and M. Kawasaki. Internal electric field effect on luminescence properties of ZnO/(Mg, Zn)O quantum wells. Physica E. 2004;21:671–675. doi:10.1063/1.3481078

[10] S. H. Park and D. Ahn. Internal field engineering in CdZnO/MgZnO quantum well structures. Applied Physics Letters. 2009;v:083507(1)–(3). doi:10.1063/1.390490.

[11] H. Teisseyre, A. Kaminska, S. Birner, T. D. Young, A. Suchocki and A. Kozanecki. Influence of hydrostatic pressure on the built-in electric field in ZnO/MgZnO quantum wells. Journal of Applied Physics. 2016;119:215702(1)–(8). doi:10.1063/1.4953251

[12] K. Sato, T. Abe, R. Fujimura, K. Yasuda, T. Yamaguchi, H. Kasada and K. Ando. Stark effects of ZnO thin films and ZnO/MgZnO quantum wells. Physica Status Solidi (c). 2012;209:1801–1804. doi:10.1002/201100592

[13] W. L. Wang, C. Y. Peng, Y. T. Ho and L. Chang. Microstructure of *a*-plane ZnO grown on $LaAlO_3$ (001). Thin Solid Films. 2010;518:2967–2970. doi:10.1016/j.tsf.2009.09.186

[14] T. Huang, S. Zhou, H. Teng, H. Lin, J. Wang, P. Han and R. Zhang. Growth and characterization of ZnO films on (001), (100) and (010) $LiGaO_2$ substrates. Journal of Crystal Growths. 2008;310:3144–3148. doi:10.1016/j.jcrsgro.2008.03.037

[15] X. H. Wei, Y. R. Li, J. Zhu, W. Huang, Y. Zhang, W. B. Luo and H. Ji. Epitaxial properties of ZnO thin films on $SrTiO_3$ substrates grown by laser molecular beam epitaxy. Applied Physics Letters. 2007;90:151918(1)–(3). doi:10.1063/1.2719026

[16] M. M. C. Chou, D. R. Hang, S. C. Wang, C. Chen, S. C. Wang and C. Y. Lee. Nonpolar *a*-plane ZnO growth and nucleation mechanism on (100) (La, Sr) (Al, Ta)O_3 substrate. Materials Chemistry and Physics. 2011;125:791–795. doi:10.1016/j.atchemphys.2010.09.057

[17] C. Y. Peng, J. S. Tian, W. L. Wang, Y. T. Ho and L. Chang. Morphology evolution of *a*-plane ZnO films on *r*-plane sapphire with growth by pulsed laser deposition. Applied Surface Science. 2013;265:553–557. doi:10.1016/j.apsusc.2012.11.044

[18] S. K. Han, S. K. Hong, J. W. Lee, J. Y. Lee, J. H. Song, Y. S. Nam, S. K. Chang, T. Minegishi and T. Yao. Structural and optical properties of nonpolar *A*-plane ZnO films grown on *R*-plane sapphire substrates by plasma-assisted molecular-beam epitaxy. Journal of Crystal Growth. 2007;309:121–127. doi:10.1016/j.jcrysgro.2007.09.025

[19] T. Moriyama and S. Fujita. Growth behaviour of nonpolar ZnO on M-plane and R-plane sapphire by metalorganic vapor phase epitaxy. Japanese Journal of Applied Physics. 2005;44:7919–7291. doi:10.1143/JJAP.44.7919

[20] M. D. Neumann, N. Esse, J. M. Chauveau, R. Goldhahn and M. Feneberg. Inversion of absorption anisotropy and bowing of crystal field splitting in wurtzite MgZnO. Applied Physics Letters. 2016;108:221105(1)–(4). doi:10.1063/1.4953159

[21] H. Lin, H. J. Su, C. H. Lu, C. P. Chang, W. R. Liu and W. F. Hsieh. Pump polarization dependent ultrafast carrier dynamics and two-photon absorption in an *a*-plane ZnO epitaxial film. Applied Physics Letters. 2015;107:142107(1)–(4). doi:10.1063/1.4933038

[22] C. M. Lai, Y. E. Huang, K. Y. Lou, C. H. Chen, L. W. Tu and S. W. Feng. Experimental and theoretical study of polarized photoluminescence caused by anisotropic strain relaxation in nonpolar a-plane textured ZnO grown by a low-pressure chemical vapour deposition. Applied Physics Letters. 2015;107:022110(1)–(4). doi:10.1063/1.4926978

[23] S. Yang, H. C. Hsu, W. R. Liu, B. H. Lin, C. C. Kuo, C. H. Hsu, M. O. Eriksson, P. O. Holtz and W. F. Hsieh. Recombination dynamics of a localized exciton bound at basal stacking faults within the *m*-plane ZnO film. Applied Physics Letters. 2014;105:011106(1)–(5). doi:10.1063/1.4887280

[24] C. H. Chao, W. J. Weng and D. H. Wei. Enhanced UV Photodetector response and recovery times using a nonpolar ZnO sensing layer. Journal of Vacuum Science and Technology A. 2016;34:02D106(1)–(7). doi:10.1116/4939751

[25] F. J. Klüpfel, H. V. Wenckstern and M. Grundmann. Low frequency noise of ZnO based metal-semiconductor field-effect transistors. Applied Physics Letters. 2015;106:033502(1)–(4). doi:10.163/1.4906292

[26] G. Tabares, A. Hierro, M. Lopez-Ponce, E. Munoz, B. Vinter and J. M. Chauveau. Light polarization sensitive photodetectors with *m*- and *r*-plane homoepitaxial ZnO/MgZnO quantum wells. Applied Physics Letters. 2015;106:061114(1)–(3). doi:10.1063/1.4908183

[27] A. Shao, P. S. Ku, X. L. Wang, W. F. Cheng, C. W. Leung and A. Ruotolo. Growth and characterization of nonpolar, heavily Mn-substituted ZnO films. Journal of Applied Physics. 2014;115:17D703(1)–(3). doi:10.1063/1.4862846

[28] H. H. Zhang, X. H. Pan, Y. Li, Z. Z. Ye, B. Lu, W. Chen, J. Y. Huang, P. Ding, S. S. Chen, H. P. He, J. G. Lu, L. X. Chen and C. L. Ye. The role of band alignment in p-type

conductivity of Na-doped ZnMgO: Polar versus nonpolar. Applied Physics Letters. 2014;104:112106(1)–(4). doi:10.1063/1.4869481

[29] J.-M. Chauveau, M. Teisseire, H. Kim-Chauveau, C. Deparis, C. Morgain and B. Vinter. Benefits of homoepitaxy on the properties of nonpolar (Zn, Mg)O/ZnO quantum wells on a-plane ZnO substrates. Applied Physics Letters. 2010;97:081903(1)–(3). doi: 10.1063/1.3481078

[30] H. Matsui and H. Tabata. The contribution of quantum confinement to optical anisotropy of *a*-plane $Cd_{0.0}6Zn_{0.94}O$/ZnO quantum wells. Applied Physics Letters. 2012;100:171910(1)–(4). doi:10.1063/1.4707384

[31] H. Matsui, N. Hasuike, H. Harima and H. Tabata. Growth evolution of surface nanowires and large anisotropy of conductivity on MgZnO/ZnO quantum wells based on M-nonpolar (10–10) ZnO. Journal of Applied Physics. 2008;104:094309(1)–(6). doi: 10.1063/1.3009959

[32] T. S. Ko, T. C. Lu, L. F. Zhuo, W. L. Wang, M. H. Liang, H. C. Kuo, S. C. Wang, L. Chang and D. Y. Lin. Optical characteristics of a-plane $Zn/Zn_{0.8}Mg_{0.2}O$ multiple quantum wells grown by pulse laser deposition. Journal of Applied Physics. 2010;108:073504(1)–(3). doi:10.1063/1.3488898

[33] G. Tabares, A. Hierro, B. Vinter and J.-M. Chauveau. Polarization-sensitive schottky photodiodes based on *a*-plane ZnO/ZnMgO multiple quantum wells. Applied Physics Letters. 2011;99:071108(1)–(3). doi:10.1063/1.3624924

[34] Z. Zhang, H. V. Wenckstern, J. Lenzner and M. Grundmann. Wavelength-selective ultraviolet (Mg, Zn)O photodiodes: Tuning of parallel composition gradients with oxygen pressure. Applied Physics Letters. 2016;108:243503(1)–(4). doi: 10.1063/1.4954375

[35] K. H. Baik, H. Kim, J. Kim, S. Jung and S. Jang. Nonpolar light emitting diode with sharp near-ultraviolet emissions using hydrothermally grown ZnO on p-GaN. Applied Physics Letters. 2013;103:091107(1)–(4). doi:10.1063/1.4819847

[36] V. Awasthi, S. K. Pandey, V. Garg, B. S. Brajendra, S. Sengar and P. Sharma. Plasmon generation in sputtered Ga-doped MgZnO thin films for solar cell applications. Journal of Applied Physics. 2016;119:233101(1)–(12). doi:10.1063/1.4953877

[37] D. C. Reynolds, D. C. Look, B. Jogai, C. W. Litton, G. Cantwell and W. C. Harsch. Valence-band ordering in ZnO. Physical Review B. 1999;60:2340–2344. doi:10.1103/Phys.RevB.60.2340

[38] H. Matsui and H. Tabata. In-plane anisotropy of polarized photoluminescence in *M*-plane (10–10) ZnO and MgZnO/ZnO multiple quantum wells. Applied Physics Letters. 2009;94:161907(1)–(3). doi:10.1063/1.3124243

[39] H. Matsui and H. Tabata. In-plane light polarization in nonpolar *m*-plane $Cd_xZn_{1-x}O$/ZnO quantum wells. Applied Physics Letters. 2011;98:261902(1)–(3). doi: 10.1063/1.3603931

[40] P. Misra, Y. J. Sun, O. Brandt, H. T. Grahn. In-plane polarization anisotropy and polarization rotation for M-plane GaN films on $LiAlO_2$. Applied Physics Letters. 2003;83:4327–4329. doi:10.1063/1.1630168

[41] J. Wraesinski and D. Frohlich. Two-photon and three-photon spectroscopy of ZnO under uniaxial stress. Physical Review B. 1997;56:13087–13093. doi:10.1103/PhysRevB. 56.13087

[42] W. R. L. Lambrecht, A. V. Rodina, S. Limpikumnong, B. Segall and B. K. Meyer. Valence-band ordering and magneto-optic exciton fine structure in ZnO. Physical Review B. 2002;65:075207(1)–(12). doi:10.1103/PhysRevB.65.075207

[43] S. F. Chichibu, T. Sota, G. Cantwell, D. B. Wason and C. W. Litton. Polarized photoreflectance spectra of excitonic polaritons in a ZnO single crystal. Journal of Applied Physics. 2003;93:756–758. doi:10.1063/1/1527707

[44] A. Ohtomo, M. Kawasaki, I. Ohkubo, H. Koinuma, T. Yasuda and Y. Segawa. Structural and optical properties of ZnO/$Mg_{0.2}Zn_{0.8}O$ superlattices. Applied Physics Letters. 1999;75:980–982. doi:10.1063/1/124573

[45] H. Karzel, W. Potzel, M. Kofferlein, W. Schiessl, M. Steiner, U. Hiller, G. M. Kalvius, D. W. Mitchell, T. P. Das, P. Blaha, K. Schwarz and M. P. Pasternak. Lattice dynamics and hyperfine interactions in ZnO and ZnSe at high external pressures. Physical Review B. 1996;53:11425–11438. doi:10.1103/PhysRevB.53.11425

[46] H. H. Huang and Y. R. Wu. Study of polarization properties of light emitted from a-plane InGaN/GaN quantum-well-based light emitting diodes. Journal of Applied Physics. 2009;106:023106(1)–(6). doi:10.1063/1.3176964

[47] T. B. Bateman. Elastic moduli of single-crystal zinc oxide. Journal of Applied Physics. 1962;33:3309–3312. doi:10.1063/1.1931160

[48] S. Ghosh, P. Waltereit, O. Brandt, H. T. Grahn and K. H. Ploog. Electronic band structure of wurtzite GaN under biaxial strain in the M-plane investigated with photoreflectance spectroscopy. Physical Review B. 2002;65:075202(1)–(7). doi:10.1103/PhysRevB. 65.75202

[49] V. A. Fonoberov and A. A. Balandin. Excitonic properties of strained wurtzite and zinc-blende GaN/Al_xGa_{1-x} N quantum dots. Journal of Applied Physics. 2003;94:7178–7183. doi:10.1063/1.1623330

[50] M. Suzuki and T. Uenoyama. Theoretical study of momentum matrix elements of GaN. Japanese Journal of Applied Physics. 1996;35:543–545.

[51] H. Matsui and H. Tabata. Engineering of optical polarization based on electronic band structures of A-plane ZnO layers under biaxial strains. Journal of Applied Physics. 2014;116:113505(1)–(7). doi:10.1063/1.4895842

[52] V. Darakchieva, T. Paskova, M. Schubert, H. Arwin, P. P. Paskov, B. Monemar, D. Hommel, M. Heuken, J. Off, F. Scholz, B. A. Haskell, P. T. Fini, J. S. Speck and S. Nakamura. Anisotropic strain and phonon deformation potentials in GaN. Physical Review B. 2007;75:195217(1)–(11). doi:10.1103/PhysRevB.75.195217[26]

[53] H. Matsui and H. Tabata. Lattice strains and polarized luminescence in homoepitaxial growth of *a*-plane ZnO. Applied Physics Letters. 2012;101:231901(1)–(4). doi:10.1063/1.4769036

[54] O. Dulub, L. Boatner and U. Diebold. STM study of the geometric and electronic structure of ZnO (0001)-Zn, (000–1)-, (10–10) and (11–20) surfaces. Surface Science. 2002;519:201–217.

[55] A. Ishii, Y. Oda and K. Fujiwara. DFT study for the anisotropic epitaxial growth of a-face ZnO (11–20). Physcia Status Solidi (c). 2008;5:2726–2728. doi:10.1002/pssc200779288DFT (study for the anisotropic epitaxial growth of a-face ZnO(1120)).

[56] H. Matsui and H. Tabata. Self-organized nanostripe arrays on ZnO (10–10) surfaces formed during laser molecular-beam-epitaxy growth. Applied Physics Letters. 2005;87:143109(1)–(3). doi:10.1063/1.2081133

[57] H. Matsui and H. Tabata. Correlation of self-organized surface nanostructures and anisotropic electron transport in nonpolar ZnO (10–10) homoepitaxy. Journal of Applied Physics. 2006;99:124307(1)–(8). doi:10.1063/1.2207551

[58] K. Kojima, H. Kamon, M. Funato and Y. Kawakami. Theoretical investigations on anisotropic optical properties in semipolar and nonpolar InGaN quantum wells. Physcia Status Solidi (c). 2008;5:3038–3041. doi:10.1002/pssc200779277

[59] H. Matsui, T. Osone and H. Tabata. Band alignment and excitonic localization of ZnO/$Cd_{0.8}Zn_{0.92}O$ quantum wells. Journal of Applied Physics. 2010;107:093523(1)–(6). doi:10.1063/1.3359720

[60] T. Makino, Y. Segawa, M. Kawasaki, A. Ohtomo, R. Shiroki, K. Tamura, T. Yasuda and H. Koinuma. Band gap engineering based on $Mg_xZn_{1-x}O$ and $Cd_yZn_{1-y}O$ ternary alloy films. Applied Physics Letters. 2001;78:1237–1239. doi:10.1063/1.1350632

[61] R. Mata, A. Cros, J. A. Budagosky, A. Molina-Sanchez, N. Garro, A. Garcia-Cristobal, J. Renard, S. Founta, B. Gayral, E. Bellet-Amalric, C. Bougerol and B. Daudin. Reversed polarized emission in highly

strained a-plane GaN/AlN multiple quantum wells. Physical Review B. 2010;82:125405(1)–(9). doi:10.1103/PhysRevB.82.125405

[62] C. G. Tang, Y. H. Chen, B. Xu, X. L. Ye and Z. G. Wang. Well-width dependence of in-plane optical anisotropy in (001) GaAs/AlGaAs quantum wells induced by in-plane uniaxial strain and interface asymmetry. Journal of Applied Physics. 2009;105:103108(1)–(6). doi:10.1063/1.3132089

IntechOpen

IntechOpen